ROYAL SOCIETY OPEN SCIENCE

royalsocietypublishing.org/journal/rsos

Research

Cite this article: Vallejo W, Rueda A, Díaz-Uribe C, Grande C, Quintana P. 2019 Photocatalytic activity of graphene oxide–TiO_2 thin films sensitized by natural dyes extracted from *Bactris guineensis*. *R. Soc. open sci.* **6**: 181824. http://dx.doi.org/10.1098/rsos.181824

Received: 5 November 2018
Accepted: 14 January 2019

Subject Category:
Chemistry

Subject Areas:
materials science/physical chemistry

Keywords:
photocatalysis, TiO_2, graphene oxide, sensitization, natural dyes

Author for correspondence:
William Vallejo
e-mail: williamvallejo@mail.uniatlantico.edu.co

†Present address: Universidad del Atlántico, Carrera 30 # 8-49, Puerto Colombia, Atlántico 081007, Colombia.

This article has been edited by the Royal Society of Chemistry, including the commissioning, peer review process and editorial aspects up to the point of acceptance.

THE ROYAL SOCIETY PUBLISHING

Photocatalytic activity of graphene oxide–TiO_2 thin films sensitized by natural dyes extracted from *Bactris guineensis*

William Vallejo[1,†], Angie Rueda[1], Carlos Díaz-Uribe[1], Carlos Grande[1] and Patricia Quintana[2]

[1]Grupo de Fotoquímica y Fotobiología, Universidad del Atlántico, 081007 Puerto Colombia, Colombia
[2]Centro de Investigación y de Estudios Avanzados del IPN, CINVESTAV, Unidad Mérida, 97310 Mérida, YUC, México

WV, 0000-0002-6661-545X

This study synthesized and characterized composites of graphene oxide and TiO_2 (GO–TiO_2). GO–TiO_2 thin films were deposited using the doctor blade technique. Subsequently, the thin films were sensitized with a natural dye extracted from a Colombian source (*Bactris guineensis*). Thermogravimetric analysis, X-ray diffraction, Raman spectroscopy, scanning electron microscopy (SEM), X-ray photoelectron spectroscopy (XPS) and diffuse reflectance measurements were used for physico-chemical characterization. All the samples were polycrystalline in nature, and the diffraction signals corresponded to the TiO_2 anatase crystalline phase. Raman spectroscopy and Fourier transform infrared spectroscopy (FTIR) verified the synthesis of composite thin films, and the SEM analysis confirmed the TiO_2 films morphological modification after the process of GO incorporation and sensitization. XPS results suggested a possibility of appearance of titanium (III) through the formation of oxygen vacancies (O_v). Furthermore, the optical results indicated that the presence of the natural sensitizer and GO improved the optical properties of TiO_2 in the visible range. Finally, the photocatalytic degradation of methylene blue was studied under visible irradiation in aqueous solution, and pseudo-first-order model was used to obtain kinetic information about photocatalytic degradation. These results indicated that the presence of GO has an important synergistic effect in conjunction with the natural sensitizer, reaching a photocatalytic yield of 33%.

1. Introduction

In recent decades, the increased concentration of organic dyes in water has been a problem of growing concern; the textiles, paper and plastics industries use dyes in the manufacture of their products and consume a large quantity of water, increasing quantities of these pollutants in the final effluent [1,2]. Recent studies have demonstrated that heterogeneous photocatalysis is a promising technology as an alternative for water purification, especially in reducing the concentration of dyes in wastewater by the use of different kinds of semiconductors under a specific radiation source [3–5]. Nowadays, titanium dioxide (TiO_2) has been broadly used as an efficient photocatalyst for environmental applications for both air and water purification due to its great quality/price ratio, chemical stability, good optical transparency and non-toxicity [5–7]. However, TiO_2 has two drawbacks: (i) it is photocatalytically active under ultraviolet irradiation ($\lambda <$ 350 nm) due to its high band gap energy value (3.2 eV) and (ii) low quantum efficiency in charge-carrier generation [8]. Many methods have been developed to increase or extend TiO_2 photo-activity in the visible light region: (i) preparing micro and nanostructures (e.g. spheres and three-dimensional hierarchical) using different synthesis methods (e.g. CVD, CBD, solvothermal, sol–gel, template-free process and spray pyrolysis) [9–11], (ii) doping TiO_2 structure with other atoms (e.g. Cu, Co, Ni, Cr, Mn, Mo, Nb, V, Fe, S, N, C, P and I) [12–14], (iii) surface plasmon resonance (e.g. Ag/TiO_2, Au/TiO_2 and Pt/TiO_2) [15], (iv) coupled semiconductor (e.g. $CaTe/TiO_2$, CdS/TiO_2, Bi_2WO_6 and ZnS/TiO_2) [16–18], and (e) dye sensitization. Among these, one of the methods most studied for TiO_2 modification is dye sensitization [19]. Different types of dyes are reported as sensitizers of TiO_2 such as ruthenium complex, chlorophyll derivatives, natural porphyrins and others for both energetic and photocatalytic applications [20,21]. In the last decade, natural dyes have become an important source of dyes; Yuvapragasam *et al*. [22] synthesized and sensitized TiO_2 nanorods with natural dyes extracted from *Sesbania grandiflora* flowers, *Camellia sinensis* leaves and *Rubia tinctorum* roots for dye-sensitized solar cells (DSSC) fabrication. Sathyajothi *et al*. [23] reported an investigation of two types of pigments as natural photosensitizers of TiO_2 in DSSC, reporting henna (efficiency 1.08%) and beetroot (efficiency 1.3%) for each extract. Despite all the applications of natural dyes in solar cell systems, their use is limited as sensitizers for water purification. Buddee *et al*. [24] sensitized TiO_2 with curcumin natural extract for enhanced photodegradation of dyes under visible light. Additionally, Zyoud *et al*. [25] sensitized TiO_2 particles with anthocyanin for photodegradation of methyl orange, showing a complete dye mineralization under solar simulator radiations. Recent study has reported the improvement of the photocatalytic activity of TiO_2 using *Syzygium cumini* as a natural sensitizer [26]. In Colombia, there are varieties of plants whose chemical constituents could satisfy the requirements for photocatalytic applications as sensitizers, the species *Bactris guineensis* called 'corozo' is a wild palm, which grows in Central/South America and is an important source of anthocyanins [27]. The modification of semiconductors with electron-donating materials (e.g. graphene, graphene oxide (GO) and other carbon materials) is another approach to improving the catalyst efficiency. This kind of donating materials reduces the recombination rate of electron–hole pairs by increasing the charge-carrier mobility [28]. Graphene sheets, nanotubes and nanoparticles with a higher specific surface area and excellent electronic properties can be used as a photocatalytic support for TiO_2 to improve the photocatalytic activity [29]. Gunnagol *et al*. [30] obtained TiO_2–graphene nanocomposites to study the photocatalytic degradation of Rhodamine B under UV irradiation (degradation yield 98%) and under visible light irradiation (degradation yield 87.19%), and reported that this activity was reached due to the large surface area, providing a greater number of surface active sites in the materials. Yang *et al*. [31] successfully prepared TiO_2/graphene porous composites for methylene blue photodegradation, compared composites results to TiO_2 Degussa P25 and verified that the composites increased light-absorbing capacity accelerating the separation of electrons and holes, suppressing the charge recombination owing to graphene properties. Finally, Stengl *et al*. [32] obtained TiO_2/graphene nanocomposites by thermal hydrolysis of suspension with graphene nano-sheets, and titania-peroxo complex provided a good photocatalytic activity in the decomposition of butane under UV and visible light.

The present study demonstrated photocatalytic properties for structured composites based on TiO_2/GO/natural dye extract.

2. Material and methods

2.1. Natural dyes extraction

The samples of the fruit *B. guineensis* (CO) were collected in the municipality of El Banco in the Department of Magdalena, Colombia (geographical location, latitude: 9°00′03″ N, longitude: 73°58′28″ W to 25 m above sea

level). In natural dye extraction, the fruit was placed inside a percolator with an ethanol : water mixture (1 : 3), and the sample was acidified with HCl. The percolation process remained recirculating for 3 days. After that, distillation performed under reduced pressure was carried out to obtain crude dry extract.

2.2. TO_2/graphene oxide composites synthesis

The GO used in this study was synthesized using the modified Hummer's method. Detailed information about the preparation and characterization of the GO used in this study can be found in a recently published study [33,34]. TiO_2–GO catalysts were prepared by the sol–gel method. Titanium (IV) tetraisopropoxide (TTIP) was added very slowly in a mixture of isopropyl alcohol in acidic medium and the corresponding concentration of the GO dispersion previously performed by ultrasound. After that, hydrolysis was applied in reflux equipment controlling the temperature. The precipitate was dried at 120°C overnight and then calcined in air at 500°C for 4–5 h [35]. Finally, solid TiO_2 with GO 0.15, 0.26, 0.51 and 1.1 (w/w %) were obtained; the samples were named A-TiO_2–GO, B-TiO_2–GO, C-TiO_2–GO and D-TiO_2–GO, respectively.

2.3. TO_2/GO composites sensitization

TiO_2–GO powder was mixed and macerated with polyethylene glycol and isopropyl alcohol at acidic pH and vigorously stirred to form a fine suspension. After that, the thin films were deposited on a glass substrate using the doctor blade method, and the film thickness was measured using a Veeco Dektak 150 profilometer (6 µm of thickness). The thin films were heated at 500°C for 1 h. For natural dye sensitization of the TiO_2–GO thin films, the coatings were immersed in a solution at pH 3 of the previously extracted dye. The adsorption process was carried out for 24 h in constant agitation; after that, the sensitized film was washed and dried at room temperature.

2.4. TO_2/GO composites characterization

The thermal decomposition behaviour of the compounds was studied by thermogravimetric analysis (TGA Discovery) in a range of 30–900°C with a nitrogen atmosphere and a ramp of 10°C min^{-1}. Studies on adsorption–desorption of H_2 at high pressure at 77.48 K and up to 6000 kPa were carried out in a high-pressure gas adsorption device (BELSORP MAX-LP, BEL Japan, Inc.). The optical properties of the thin films were analysed by the diffuse reflectance technique using a deuterium–halogen source (Mod. AvaLight DH-S-BAL) and an AvaSpec-2048 optical fibre coupled to a bifurcated fibre (FCR-7UV100-2-1X25) with an AFH-Eye of Avantes at 45°. The measurements were normalized using a standard white material (Spectralon as a reflective material, which has 99% reflectivity in the range of 200 nm to 2.5 µm, Ocean Optics WS-1-SL). The surface reflectance spectra of all the samples were recorded in the visible range in several zones to obtain a representative value (the illumination point was 1 mm in diameter) [36]. The semiconductor surface modification with GO was monitored by Raman spectroscopy (Witec Alpha 300 Raman/AFM equipment) in a range of 50–3500 cm^{-1} with a length excitation laser of 488 nm and an integration time of 1.00485 s. Furthermore, in order to obtain the compounds' structural properties, an X-ray diffraction analysis was performed (Bruker D8 Advance diffractometer, Bruker AXS, Germany) using Cu–Kα radiation ($\lambda = 0.15406$ nm) under a voltage of 34 kV and a current of 25 mA. The morphological properties (size, distribution and dispersion of the particles) were analysed by scanning electron microscopy (model JSM-7600F, Jeol Ltd, Tokyo, Japan) under an excitation energy of 5 and 1 kV and samples metalized with gold–palladium for 30 s. The elemental composition was analysed by X-ray scattering spectroscopy. Modified and unmodified thin films with different GO loads were analysed by X-ray photoelectron spectroscopy (XPS). Data were obtained using the Thermo Scientific™ K-Alpha™ X-ray Photoelectron Spectrometer (ThermoFisher Scientific, USA), with a hemispheric analyser with an X-ray source from KR Al ($h\nu$) 1486.6 eV using a vacuum of approximately 10^{-7} Pa. The Avantage V. 59902 software was used in the analysis of peaks in the XPS spectra; furthermore, the decomposition of the peaks was performed with Gaussian components after a Shirley background subtraction.

2.5. Photocatalytic behaviour

This study sought to establish the GO and natural sensitization effect on the photodegradation activity of TiO_2 under visible light radiation. For this purpose, methylene blue was chosen as the pollutant model taking into account that since 2010, the International Organization for Standardization (ISO) published Standard

10678:2010 [37]. Visible light was used as energetic source to determine the real impact of modification on the TiO_2 photocatalytic properties. The thin films were immersed in blue methylene solution (25 ppm was used as target solution), and prior to irradiation, the system was magnetically stirred in the dark for 1 h to ensure the equilibrium of dye adsorption–desorption on the thin film surface. The system was irradiated by a visible lamp with an emission during 100 min. The concentration of dye was determined through the spectrophotometric method (Thermo Scientific–Genesys 10S) using 665 nm as fixed wavelength, with a calibration curve (correlation coefficient $R = 0.997$) using the Lambert–Beer equation.

3. Results and discussion

3.1. Adsorption characterization

The surface area values and pore volume obtained from the method of Brunauer–Emmett–Teller (BET) and the adsorption and desorption isotherms are shown in figure 1. The specific surface area and total pore volume of the prepared composites are listed in table 1. The results of the BET analysis showed that composites had pore size around (8.06–9.23 nm), which are considered mesoporous composites according to IUPAC notation (mesoporous materials include the range of pore diameters between 2 and 50 nm); furthermore, the isotherms shown in figure 1 have the behaviour of type IV isotherms attributed to mesoporous solids [38]. Table 1 shows that, as GO concentration increases in the composite, the specific surface area decreases. According to data reported by Stengl *et al*. about the influence of the GO in the photocatalytic activity of TiO_2, the reduction in the surface area could be due to an agglomeration given by the carbonaceous material, in which the GO is completely covered by semiconductor particles. Consequently, when it is required to measure the surface area of the modified materials, this depends mainly on the surface properties that present the anatase particles in the material [32].

3.2. TGA characterization

The thermal analysis and the stability of the catalysts were determined by TGA. Figure 2 shows the TGA curves for compounds. The unmodified TiO_2 shows two stages of mass loss: (i) the first stage between 30 and 150°C with mass loss percentage of 2.96%—this change is associated with the evaporation of both water and solvent (isopropanol) molecules adsorbed on the surface of the material; (ii) second mass loss between 390 and 800°C with a loss percentage of 5.5%—this change is typical of the formation and reorganization of rutile phase crystalline structure (600–750°C); such results are in line with reports in the literature [39].

In relation to the modified samples (A-TiO_2–GO, B-TiO_2–GO, C-TiO_2–GO and D-TiO_2–GO), figure 2 shows three stages of mass loss: (i) the first stage is localized between 30 and 200°C with a loss percentage of 2.95%—this change is attributed to the evaporation of the water and solvent molecules present on the material surface [40]; (ii) the second stage is localized between 200 and 350°C with an average percentage of 0.74%—this mass loss corresponds to the removal of oxygen molecules contained in the labile functional groups (hydroxyl and carboxyl) present in the GO structure; at temperatures close to 350°C, the GO loses more stable oxygenated groups like carbonyls on the edge of GO sheets [41]; (iii) the last stage of change is localized between 450 and 800°C with a mass loss percentage of 4.14%—this stage is associated with the GO breakdown, the catalytic surface dehydroxylation and carbon substrate combustion (the carbon skeleton pyrolysis); furthermore, the formation and reorganization rutile phase occurs between 600 and 750°C [42]. For the sample D-TiO_2–GO, two stages of weight loss were very resilient, with a loss percentage greater than the other three modified samples. This result can be attributed to the greater concentration of GO present in this sample; this greater proportion implies greater abundance of labile oxygen functional groups attached to the surface in its hexagonal structure, leading to greater mass losses in the second and third stages of the process [43].

3.3. Raman spectroscopy characterization

Figure 3 shows the Raman spectra of synthesized materials. All samples showed a similar pattern characteristic to the TiO_2 anatase phase peak; the structure of the semiconductor anatase phase has six Raman active modes [44,45]:

$$\text{anatase} = A_{1g} + 2B_{1g} + 3E_g. \tag{3.1}$$

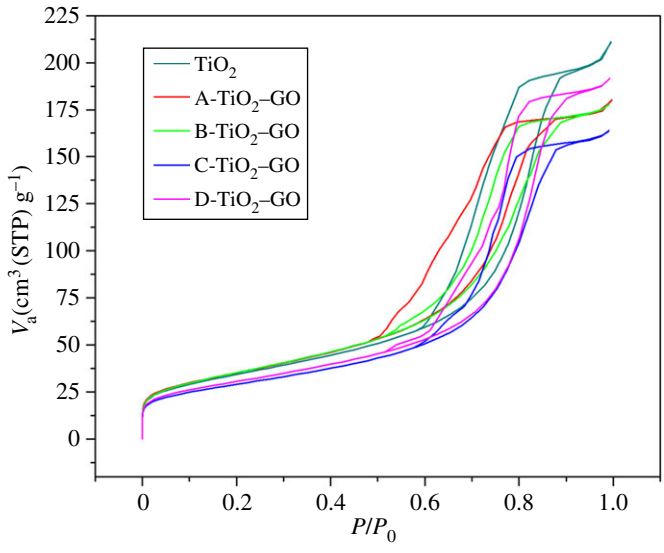

Figure 1. N_2 adsorption and desorption isotherms for unmodified TiO_2, A-TiO_2–GO, B-TiO_2–GO, C-TiO_2–GO and D-TiO_2–GO.

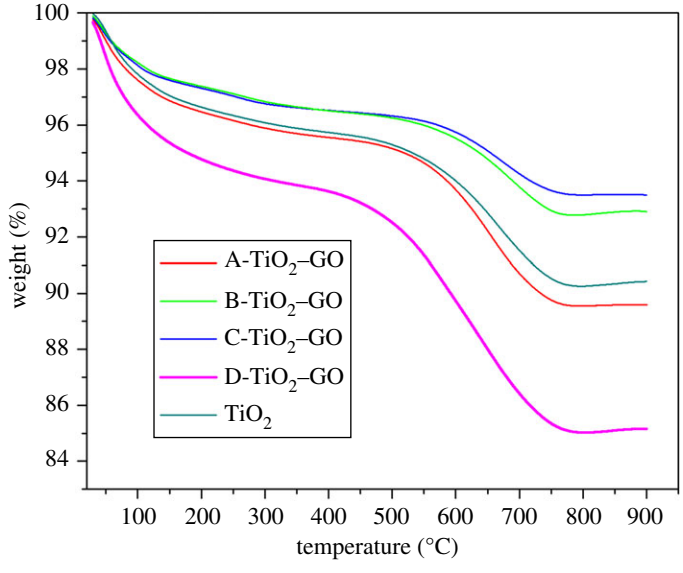

Figure 2. TGA curves for synthesized materials.

Table 1. BET and total pore volume of the prepared samples.

catalysts	specific surface area ($m^2\ g^{-1}$)	total pore volume ($cm^3\ g^{-1}$)	pore size (nm)
unmodified TiO_2	123.30	0.3229	9.23
A-TiO_2–GO	126.32	0.2755	8.06
B-TiO_2–GO	128.28	0.2746	7.05
C-TiO_2–GO	104.33	0.2534	8.06
D-TiO_2–GO	109.96	0.2956	9.13

The Raman spectrum shows a strong signal localized at 145 cm^{-1}, which is caused by the external vibration of the TiO_2 anatase structure. The peaks localized at 145, 195 and 638 cm^{-1} correspond to the vibrational modes E_{1g}, and the peak localized at 398 cm^{-1} can be attributed to the B_{1g} vibration mode. Figure 3 shows the signal localized at 515 cm^{-1}, which is a double-signal corresponding to the modes A_g

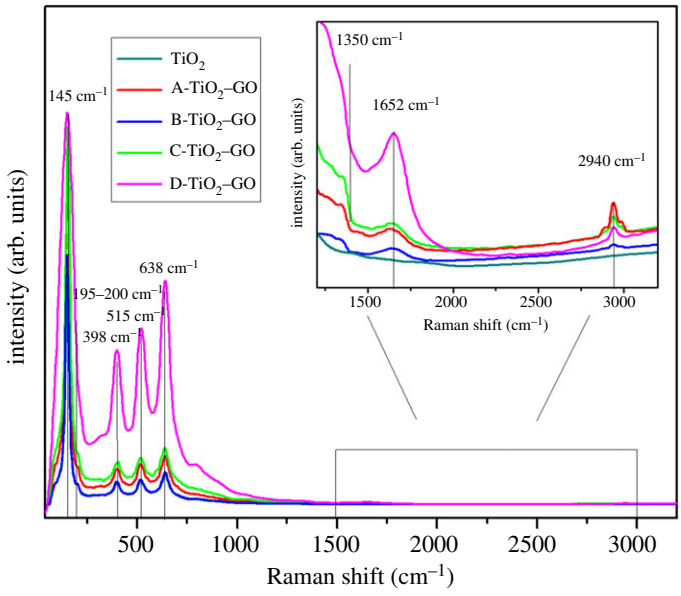

Figure 3. Raman spectra for the synthesized materials.

and B_{1g}. Finally, none of the Raman bands corresponding to the TiO_2 rutile phase were detected in the spectra [46–48]. For GO, two Raman active E_{2g} modes are predicted, each doubly degenerate. Furthermore, in GO samples with defects, the overall momentum conservation can be satisfied by adding an electron-defect scattering event to the process, and two processes can be presented: (i) one-phonon defect-assisted process and (ii) two-phonon defect-assisted process [49]. Inside figure 3, a plot inset in the range of 1200–3500 cm^{-1} allows verifying the presence of the characteristic signals for GO, a band localized at 1350 cm^{-1} and another band localized at 1652 cm^{-1} corresponding to bands D and G, respectively. Band D is attributed to defects of sp^3 carbons localized at the edges or in the plane of GO sheets, while band G is assigned to vibration of the atoms of carbon sp^2 ordered in the hexagonal structure inside graphene [50,51]. Finally, the bands at 2940 cm^{-1} are associated with harmonics combination for bands D and D′, which takes place through a defect-induced triple resonance process involving both 'inter-valley' and 'intra-valley' scattering processes, whose intensity increases with the amount of disorder [52].

Furthermore, figure 3 shows that the TiO_2 Raman signals enhanced after the GO content increase inside the catalysts (from TiO_2 until D-TiO_2–GO). Naumenko *et al*. [53] reported a significant electronic interaction between the TiO_2 nanoparticles deposited by chemical vapour deposition on graphene sheets, and proposed that changes in Raman peak positions and intensity ratios could be due to the charge transfer process between graphene and TiO_2 nanoparticles, and this increased the Raman signal of the TiO_2 nanoparticles several times. Other reports have suggested that Raman intensity of TiO_2 nanoparticles increased with the disorder of the graphene structure; this change in the intensities of the Raman peaks for increasing disorder has been reported for vacancies-type defects [54,55].

3.4. X-ray characterization

Figure 4 shows the X-ray diffraction patterns of the compounds. A qualitative analysis was carried out using the Diffract Suite Eva software (Bruker AXS, Germany) and the JCPDS database. The diffraction patterns indicate that films had a polycrystalline structure. Furthermore, the diffraction signals corresponded to the TiO_2 anatase crystalline phase (JCPDS #021–1272). Figure 4 shows that the samples grown in a preferential crystalline plane were localized at $2\theta = 25.5^{\circ}$; this signal corresponds to the plane (101). This result corroborates the information obtained from the Raman characterization.

Figure 4 shows that after the modification process, the diffraction pattern did not change significantly; in addition, none of the films showed any evidence of the presence of the rutile and brookite phases [56]. This result is in line with other reports, for instance, Rasoulnezhad *et al*. [57] did not report additional signals corresponding to the presence of doped elements into XRD patterns for TiO_2 samples doped with S and Fe. The characteristic peak of GO cannot be appreciated due to the low concentration of GO used in the synthesis of the materials, which is in agreement with other reports on GO and TiO_2

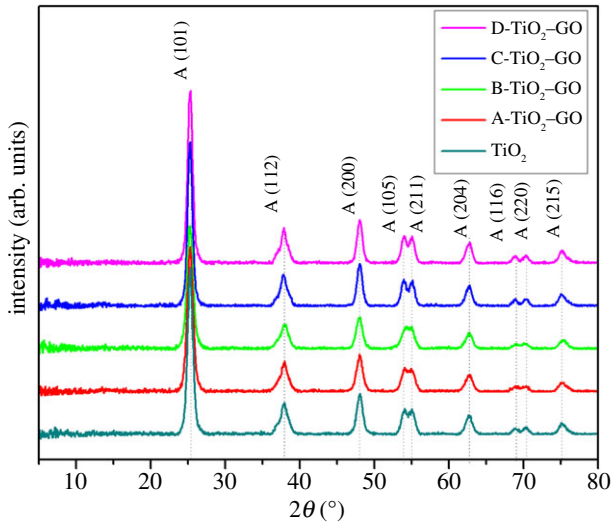

Figure 4. X-ray diffraction patterns of the composites synthesized in this study.

composites synthesis [58,59]. The crystalline domain size of the materials was calculated using the Debye–Scherrer formula and according to the preferential crystalline plane (101)

$$d_{hkl} = \frac{k\lambda}{\beta \cos(\theta)}, \tag{3.2}$$

X-ray (Cu–Kα radiation $\lambda = 0.15406$ nm), β is the diffraction angle to the full width at half maximum for the highest peak (101) and θ is the Scherrer diffraction angle [60], previous to applying the Debye–Scherrer formula, the instrumental broadening contribution was subtracted using DIFFRAC.SUITE EVA–XRD (Bruker, AXS, Germany). The average crystalline domain size obtained for all the TiO_2–GO films was near 9.63 nm, while for the unmodified TiO_2 thin films, it was 9.80 nm.

3.5. Sensitization process and FTIR characterization

After the synthesis and characterization of TiO_2–GO thin films, the thin films were sensitized with natural extract. The FTIR characterization was carried out in the range of 700–4000 cm^{-1} to verify the type of chemical bonds present on thin films surface. Figure 5 shows the FTIR spectrum obtained for the unmodified and the modified TiO_2 thin films.

Figure 5*a* shows a broad band in the range from 3500 to 3000 cm^{-1} and a band at 1672 cm^{-1}, which are typical bands of both strain and bending of O–H bonds, and are attributed to the interaction of adsorbed water molecules on the thin films surface [61]. For TiO_2–GO thin films, an intense wide band near 3200 cm^{-1} is observed, which increases in intensity as the concentration of GO increases in all the modified samples. This band could be attributed to the O–H stretching of the molecules of water absorbed on the catalyst surface and the hydroxyl groups present in the GO network—this behaviour was observed in all modified materials [62]. Furthermore, a weak band localized at 2335 cm^{-1} is assigned to O–C=O bonding, which are bonds present in the hexagonal GO. Another band is observed at 1638 cm^{-1}, whose signal is assigned to the O–H bending of water molecules and C=C strain on the aromatic ring of GO. It is possible to observe a band at 1136 cm^{-1} which corresponds to the C–O bond of the epoxy groups, and a band at 1046 cm^{-1} can be assigned to =C–H bond stretching and C–OH strain for the alkoxy groups in the GO sheets [63]. Figure 5*b* shows the FTIR spectrum for the TiO_2–GO films sensitized with anthocyanins extracted from corozo fruits (*B. guineensis*). The characteristic bands assigned to the O–H bond strain are observed. The bands localized at 2900, 2100 and 1638 cm^{-1} can be assigned to the vibrations of C–H bond, the C=O strain and the vibration of C=C conjugates of both the GO sheets and the anthocyanin structure of the natural dye, respectively. Figure 5*b* shows a typical band localized at 1430 cm^{-1} due to the OH–CH_2 bonds of the phenolic rings present in the anthocyanins. The bands around 1300 and 1060 cm^{-1} are assigned to the asymmetric and symmetrical vibration of the C–O bond of the functional ether-type groups in the anthocyanins. This band is more intense for TiO_2–sensitizers film

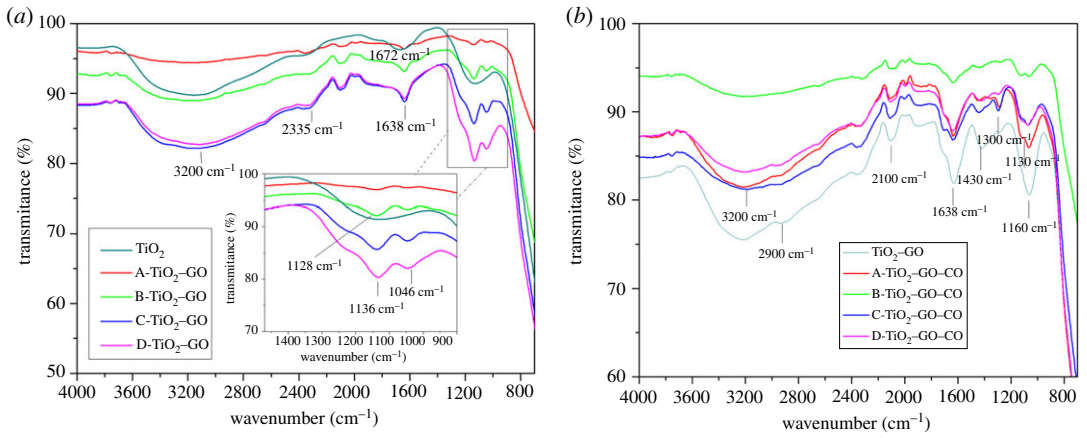

Figure 5. (*a*) FTIR spectra of the unmodified TiO_2 and TiO_2-GO photocatalysts. (*b*) FTIR spectra of TiO_2 and TiO_2-GO sensitized with natural extract.

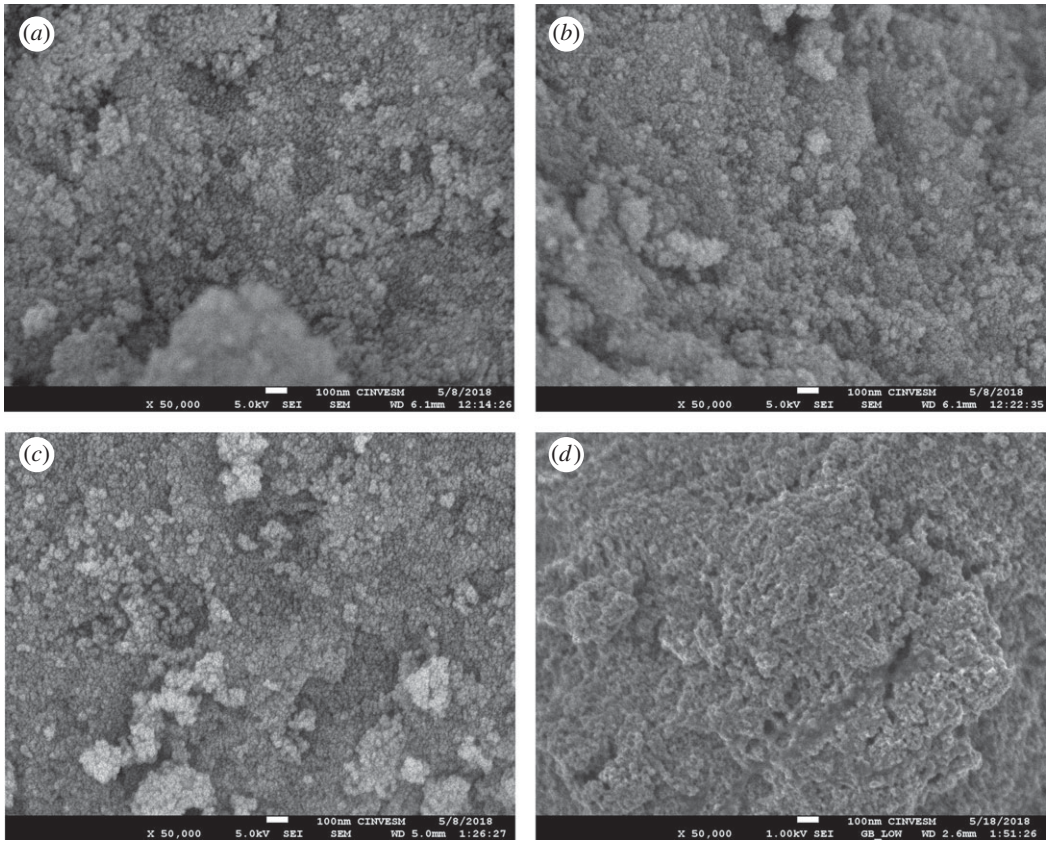

Figure 6. SEM images ×50 000: (*a*) TiO_2, (*b*) A-TiO_2-GO, (*c*) D-TiO_2-GO and (*d*) D-$TiO_2-GO-CO$.

than for TiO_2–GO–sensitizer thin films, indicating a greater absorption of the natural dye on the semiconductor surface [64,65].

3.6. Morphological characterization

Figure 6 shows SEM images with four TiO_2 thin films. Figure 6*a* shows that the TiO_2 films were formed by micro-aggregates with a narrow size margin of 15 nm. Figure 6*b*,*c* shows that, as the concentration of GO increased, agglomeration also increased. The agglomeration process is commonly reported when

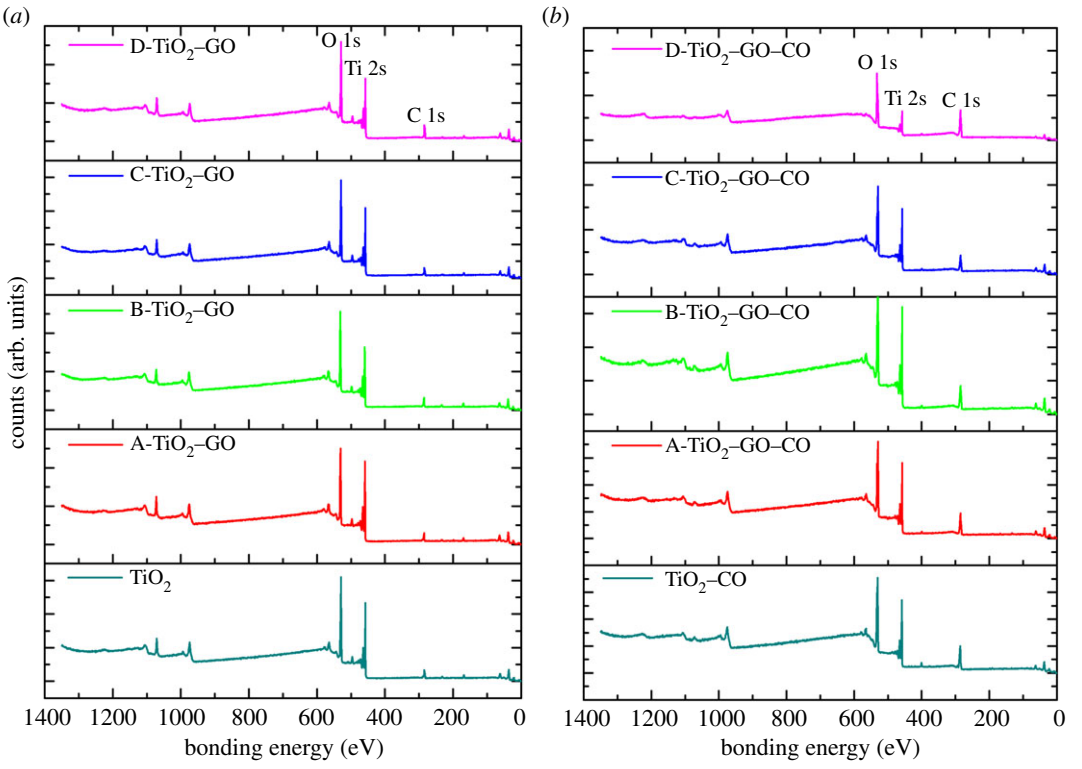

Figure 7. XPS spectrum of: (*a*) TiO_2–GO thin films and (*b*) TiO_2–GO thin films sensitized with anthocyanins extracted from the fruit of *B. guineensis*.

TiO_2 nanoparticles are combined with graphene sheets. The agglomerates of TiO_2 could enhance the photocatalytic activity because the photogenerated charge pairs can be efficiently separated through the inter-particle charge transfer within the agglomerates [66,67]. Furthermore, Ryu *et al*. [68] reported that rGO–TiO_2 agglomerates promoted CH_3CHO oxidation. Finally, figure 6*d* shows an agglomeration reduction in the particles on the surface after natural sensitization, owing to the fact that the natural dye adsorption on the catalyst surface improves the morphology of the films.

3.7. XPS thin films characterization

Figure 7 shows the XPS spectra obtained by all the synthesized films in the present study, and the spectra show the typical peaks for the elements C 1s, Ti 2p and O 1s corresponding to the bonding energy values localized at 284.5, 458 and 530 eV, respectively [69]. Figure 7*a* shows an increase in the signal for O 1s and C 1s as the concentration of GO increases in the samples, indicating a greater atomic percentage for these elements compared to the other samples—this is directly related to the concentration of graphene incorporated into the catalyst [70]. Figure 7*b* shows the spectra of the modified films with GO sensitized with anthocyanins extracted from *B. guineensis*, showing greater intensity in the peaks C 1s and O 1s, attributed to the extra contribution of these atoms by the anthocyanins from the fruit, which has an abundance of oxygen and carbon in its chemical structure, in addition to the contribution of GO [71]. In order to verify the kind of bonding in the synthesized compounds, a high-resolution XPS (HRXPS) was carried out in the specific region of (Ti 2p) for both TiO_2 and D-TiO_2–GO films (figure 8*a*). The peaks localized at 464.28 and 458.78 eV correspond to the spin-orbital splitting photoelectrons Ti $2p_{1/2}$ and Ti $2p_{3/2}$, respectively. The chemical shift of Ti $2p_{1/2}$ and Ti $2p_{3/2}$ was 5.6 eV, indicating that Ti^{4+} is present in the thin films [72]. Figure 8*a* also shows a red shift displacement of the spin to peak 0.6 eV, indicating the possibility of appearance of Ti^{3+} and that, under synthesis conditions, carbon tends to react with oxygen in the TiO_2 lattice leading to the formation of oxygen vacancies (O_v) and the low valence state of Ti^{3+} [73]. Rasoulnezhad *et al*. [74] reported the formation of Ti^{3+} species in N-doped TiO_2 thin films deposited by chemical vapour deposition. The formation of O_v and Ti^{3+} could act as electron traps and inhibit the recombination process. Furthermore, the peak ascribed to Ti–C bonds at 281 eV was not detected in the TiO_2–GO samples, which indicates that carbon was not doped into the TiO_2 lattice

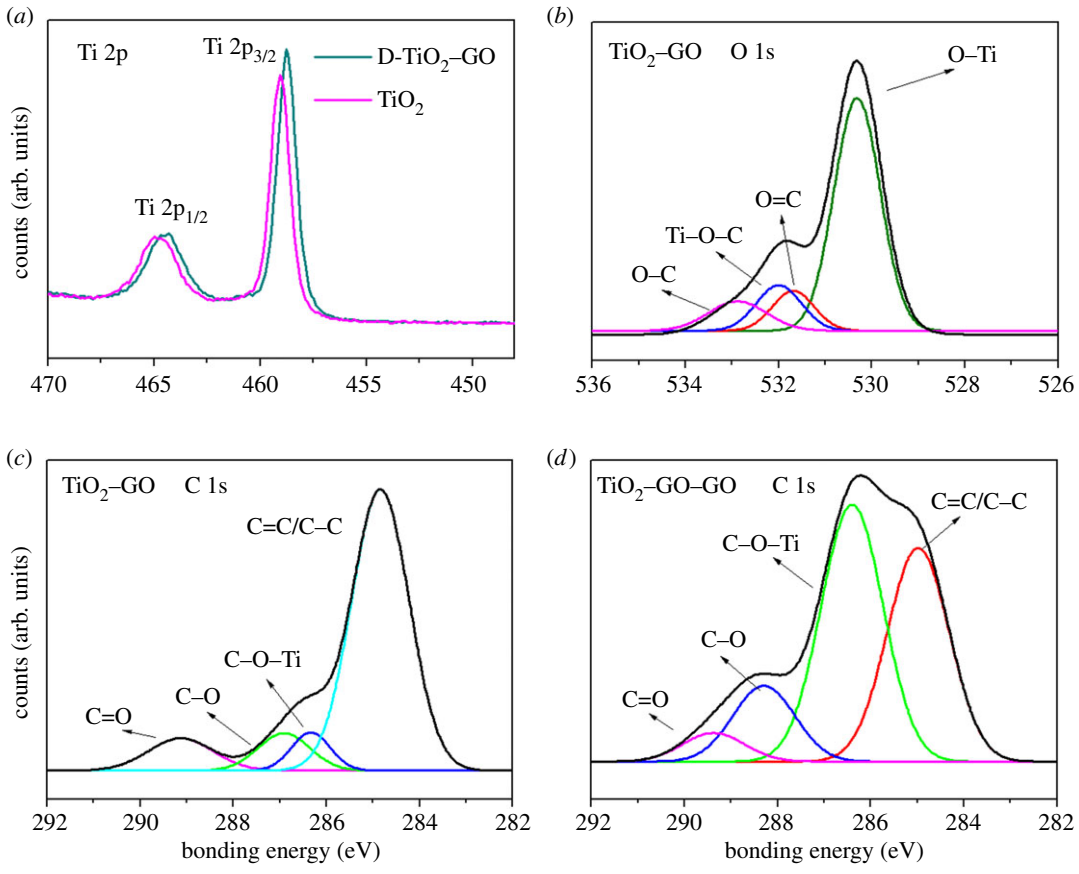

Figure 8. Peak decomposition of HRXPS to: (*a*) Ti 2p spectrum of TiO_2 and D-TiO_2−GO, (*b*) O 1s spectrum of D-TiO_2−GO thin film, (*c*) C 1s spectrum of D-TiO_2−GO and (*d*) C 1s spectrum of D-TiO_2−GO−CO.

[73,75,76]. The high-resolution spectra of O 1s and C 1s (figure 8*b*,*c*) were obtained from the sample with the highest load of GO (D-TiO_2−GO); signals that were submitted to the decomposition process. Figure 8*b* shows the HRXPS spectrum to O 1s peak, with resolution of four signals: (i) the first is centred at 530.3 eV, attributed to the O−Ti bonding of the semiconductor lattice; (ii) the peak localized at 531.6 eV corresponds to the bonds O=C and −COO of the functional GO groups; (iii) the peak localized at 531.98 eV could be assigned to the Ti−O−C bond, a signal generated by the interaction between the oxygen atoms present in the functional groups in the graphene sheet and the TiO_2 particles; (iv) the signal localized at 532.86 eV is assigned to the links C−OH and C−O−C [77,78]. Figure 8*c* shows HRXPS to element C 1s; the decomposition process of the signals shows resolution of four signals: (i) the main signal localized at 284.8 eV is assigned to carbon sp^2 (C=C) and the unhybridized sp^3 links (C−C); (ii) the second peak localized at 286.3 eV is attributed to C−O−Ti; this interaction is generated between the semiconductor and GO [79,80]. Finally, figure 8*d* shows HRXPS for the D-TiO_2−GO film sensitized with natural extract, and in these spectra, the peak localized at 286.4 eV can be assigned to interaction C−O−Ti, indicating that the anchoring of the natural sensitizer to the TiO_2 surface occurs through an interaction between semiconductor Ti and hydroxyl groups of the natural sensitizer anthocyanins; this is in line with computational studies reported on the adsorption of anthocyanins on TiO_2 clusters [26].

3.8. Optical characterization

Figure 9 shows the diffuse reflectance spectra for TiO_2, TiO_2−GO and TiO_2−GO−CO thin films. The spectra show that GO affects significantly the optical properties of TiO_2. Figure 9*a* shows a red shift of the absorption edge as GO concentration increases. The results suggest that the samples containing GO can absorb electromagnetic radiation with wavelength higher than TiO_2; absorption increased linearly with the increase in GO concentration, which indicates that GO could narrow the band gap of TiO_2 photocatalysts. For the samples sensitized with natural extract, a significant shift in the light absorption towards lengths greater than 400 nm was observed. The anthocyanins of the extract

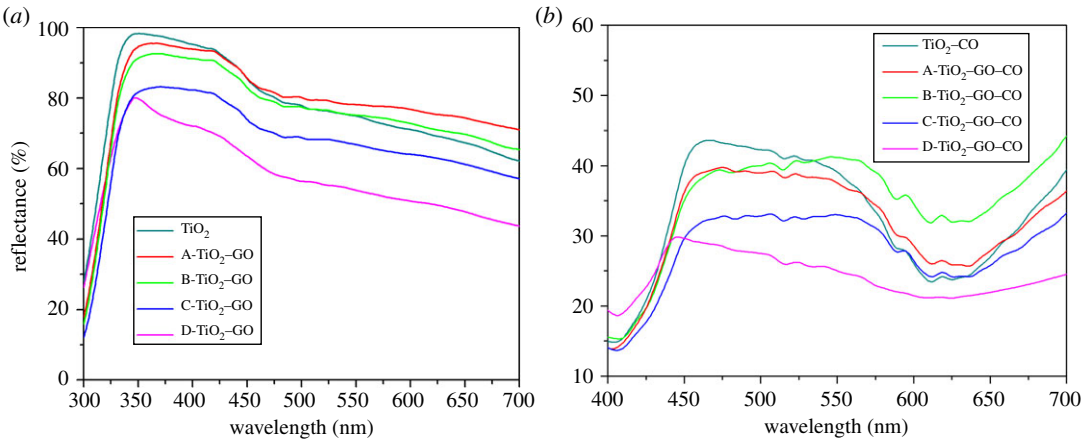

Figure 9. Reflectance diffuse spectra of: (*a*) TiO_2–GO thin films and (*b*) TiO_2–GO thin films sensitized with anthocyanins extracted from the fruit of *B. guineensis*.

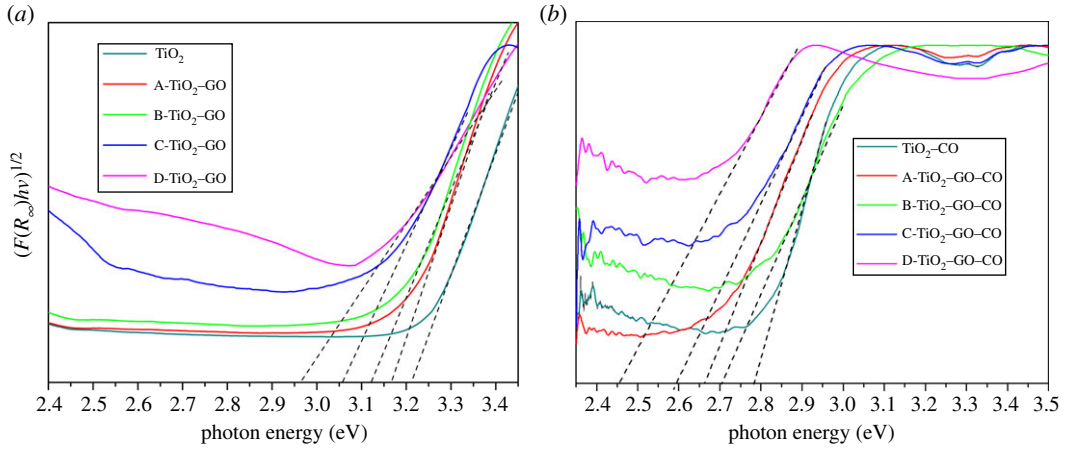

Figure 10. Kubelka–Munk plots and band gap energy estimation for: (*a*) TiO_2–GO thin films and (*b*) TiO_2–GO thin films sensitized with anthocyanins extracted from the fruit of *B. guineensis*.

contained chromophore groups into their chemical structure, which absorb in this range of the electromagnetic spectrum. This result is in line with those in other reports [81–83].

The band gap energy value was determined for all samples using the Kubelka–Munk remission function [84]

$$\frac{k}{s} = F(R_\infty) = \frac{(1 - R_\infty)^2}{2R_\infty}, \tag{3.3}$$

where R_∞ is the material reflectance value and $F(R_\infty)$ represents the ratio between the absorption and the scattering coefficients (k/s), $F(R_\infty)$ is proportional to the constant of absorption of the material, an indication of the sample absorbance at a particular wavelength. From equation (3.3) and the curves shown in figure 9, an analogue to Tauc plots $((F(R_\infty)*h\nu)^{1/2}$ against photon energy can be constructed, according to [85,86]

$$(F(R_\infty)h\nu)^{1/2} = A(h\nu - E_g). \tag{3.4}$$

Figure 10 shows plots of $(F(R_\infty)h\nu)^{1/2}$ versus $(h\nu)$ for the diffuse reflectance spectra shown in figure 9. The optical band gap of the films was determined by extrapolating the linear portion of the graph onto the *x*-axis [87]. Table 2 lists the optical properties of the thin films.

Figure 10 shows that the unmodified TiO_2 had a band gap value of 3.21 eV, which accords with reports in the literature [88,89]. The energy values for TiO_2–GO were reduced as GO concentration was increased until reaching a value of 2.96 eV for the catalyst with the highest load of GO (D-TiO_2–

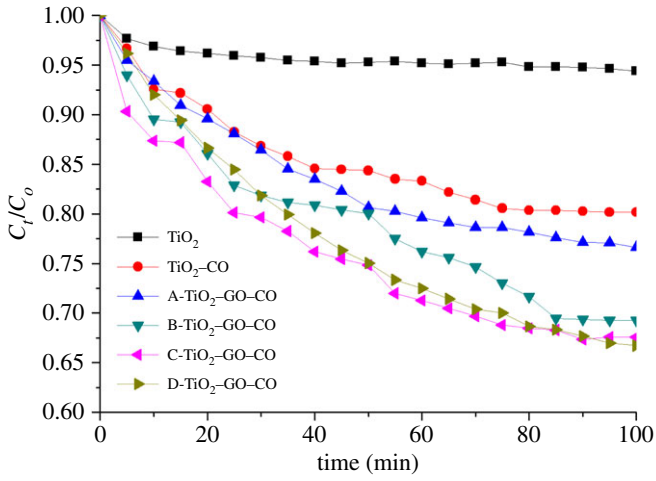

Figure 11. MB photocatalytic degradation by modified and sensitized $TiO_2-GO-CO$ materials after 100 min of visible irradiation.

Table 2. Energy band gap values for the composites synthesized.

composites	band gap (eV)	composites	band gap (eV)
unmodified TiO_2	3.21	TiO_2-CO	2.78
A-TiO_2-GO	3.16	A-$TiO_2-GO-CO$	2.66
B-TiO_2-GO	3.12	B-$TiO_2-GO-CO$	2.70
C-TiO_2-GO	3.05	C-$TiO_2-GO-CO$	2.59
D-TiO_2-GO	2.96	D-$TiO_2-GO-CO$	2.45

GO). The presence of GO allowed the generation of Ti^{3+} and O_v, and such a low valence state could generate intra-gap states with lower energy than that in the TiO_2 band gap, improving the absorption of light at higher wavelengths [73,75,90,91]. For the TiO_2–GO–CO films, a greater change in the energy band gap values was observed; an energy value of 2.78 eV was obtained for TiO_2–CO thin films up to 2.45 eV for D-TiO_2–GO–CO thin films (thin film sensitized with higher loads of graphene). The presence of a natural sensitizer significantly improves the optical properties of TiO_2–GO in the visible range of the electromagnetic spectrum, and this result is relevant to photocatalytic properties under visible irradiation [92].

3.9. Photocatalytic results

The photocatalytic activity of TiO_2–GO composites was studied by degradation of MB under visible light irradiation. TiO_2, TiO_2–CO and TiO_2–GO–CO were compared with different GO loads. Figure 11 shows the results of photodegradation for different materials. All results indicate that modifications improved the catalytic activity of the semiconductor. Furthermore, the photodegradation yield increases when the concentration of GO increases inside TiO_2 thin films. This behaviour is associated with the GO properties (e.g. electrical conductivity and capacity of charge transportation). GO sheets can promote the effective charge separation of electron–hole pair. In addition, the presence of Ti^{3+} and oxygen vacancies would facilitate the separation of charge carriers and suppress the recombination of charge carriers improving the photocatalytic activity [93,94].

Figure 11 shows that TiO_2–GO–CO films showed greater photocatalytic activity than TiO_2 films sensitized with natural extract (TiO_2–CO), which indicates that the presence of GO has an important synergistic effect in conjunction with the natural sensitizer. The presence of GO can improve the electron transport transferred from the sensitizer to TiO_2. Moreover, GO can reduce the recombination process of the photogenerated charge carrier; GO and sensitizer extend the photo-activity of TiO_2 to the visible and improve the electrical transport significantly, increasing the values of photodegradation. The

Table 3. MB degradation percentages and speed constant values for dye-sensitized TiO_2–GO thin films.

thin films	k_{app} (min^{-1})	degradation (%)
TiO_2	3.4×10^{-4}	5.61
TiO_2–CO	2.0×10^{-3}	19.82
A-TiO_2–GO–CO	2.4×10^{-3}	23.38
B-TiO_2–GO–CO	3.3×10^{-3}	30.72
C-TiO_2–GO–CO	3.5×10^{-3}	32.42
D-TiO_2–GO	3.9×10^{-3}	33.28

photodegradation kinetics of methylene blue (MB) was studied using the Langmuir–Hinshelwood kinetic model (L–H) [95,96]

$$v = -\frac{\mathrm{d}[\mathrm{AM}]}{\mathrm{d}t} = \frac{k * K[\mathrm{AM}]}{1 + K[\mathrm{AM}]}, \tag{3.5}$$

where v is the dye mineralization rate, K is the speed constant, [AM] is the concentration of methylene blue and k is the adsorption coefficient. Equation (3.5) can be explicitly resolved for (t) to use discrete changes in [AM] from the initial concentration to a zero-reference point. In the present case, an apparent first-order model can be supposed

$$v = -\frac{\mathrm{d}[\mathrm{AM}]}{\mathrm{d}t} = k_{\mathrm{app}}[\mathrm{AM}] = kK[\mathrm{AM}], \tag{3.6}$$

and

$$[\mathrm{AM}] = [\mathrm{AM}]_o \, \mathrm{e}^{-k_{\mathrm{app}}t} \, . \tag{3.7}$$

where time (t) is expressed in minutes and k_{app} ($k * K$) is the apparent reaction speed constant (min^{-1}). The k_{app} values for synthesized catalysts are listed in table 3. Results show that the natural sensitization of TiO_2 thin films increased the speed constant from a value of $3.40 \times 10^{-4}\ min^{-1}$ for the unmodified TiO_2 film to a value of $2.0 \times 10^{-3}\ min^{-1}$ in TiO_2–CO and, in this case, degradation yield increased by a factor of 4. The introduction of GO in the TiO_2 semiconductor lattice was reflected in the increase in the speed constant from a value of $3.4 \times 10^{-4}\ min^{-1}$ for the unmodified TiO_2 film to a value of $3.9 \times 10^{-3}\ min^{-1}$ for TiO_2 modified with GO, which resulted from a reduction in the recombination process and the electrical conductivity of GO. In turn, for the sensitized TiO_2–GO thin films, the k_{app} value reached higher values as GO concentration was increased in the films. The photodegradation rate was increased by 2 (D-TiO_2–GO–CO thin films) in comparison to the TiO_2 sensitized with natural extract, which indicates that the presence of GO has an important synergistic effect in conjunction with the natural sensitizer. Besides, the results suggest that the optical activity in visible range and the charge carrier's electrical transport were improved.

Rasoulnezhad *et al*. [97] reported a k_{app} value of $7.3 \times 10^{-3}\ min^{-1}$ for photocatalytic degradation of MB after 300 min under visible light irradiation using Fe-doped TiO_2 thin films as photocatalyst. In another study, Yang *et al*. [98] reported a k_{app} value of $3.3 \times 10^{-3}\ min^{-1}$ for photocatalytic degradation of MB after 180 min using poly-*o*-phenylenediamine-modified TiO_2 nanocomposites as photocatalysts. Also, Jaihindh *et al*. [99] reported a k_{app} value of $8.7 \times 10^{-3}\ min^{-1}$ for visible light photocatalytic degradation of MB after 150 min using GO-supported Ag-loaded Fe-doped TiO_2 as photocatalysts. Sohail *et al*. [100] also reported a k_{app} value of $12.2 \times 10^{-3}\ min^{-1}$ for photocatalytic degradation of MB after 120 min under UV light irradiation using TiO_2-reduced GO nanoparticles as photocatalyst. In the present study, TiO_2–GO–CO films have a suitable photocatalytic activity compared to these reports.

In order to build more knowledge in this research field, and taking into account the results presented in the previous section, a theoretical scheme of energetic levels was proposed for the material synthesized here (TiO_2–GO–CO thin films). In the first stage, natural sensitizer (S) absorbs the visible light and, after that, it is excited to a state of greater energy, leaving an electron in the lowest energy unoccupied molecular orbital (LUMO) (equation (3.8)) [101]

$$S + hv_{\mathrm{visible}} \rightarrow \quad S^*_{\mathrm{LUMO}} \tag{3.8}$$

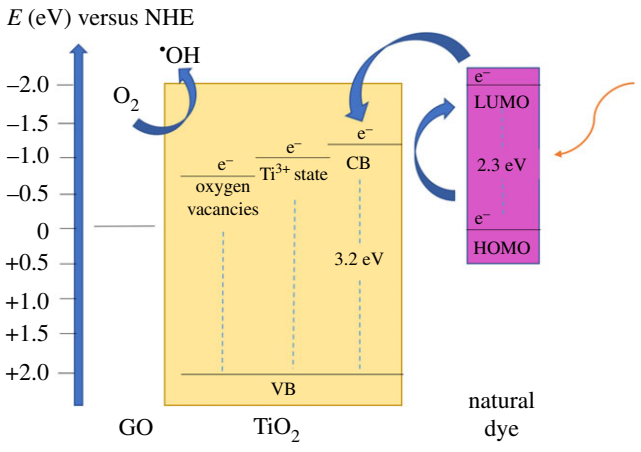

Figure 12. Scheme of energetic levels for TiO_2–GO–CO thin films: energy band gap. Localized Ti^{3+} and O_V and HOMO-LUMO transition to natural dye [73].

and

$$S^*_{\mathrm{LUMO}} + \mathrm{TiO_2} \rightarrow \ S^+ + \ \mathrm{TiO_2}(e^-_{\mathrm{CB}}). \tag{3.9}$$

This electron can be transferred to the conduction band of TiO_2 (equation (3.9)). At this point, Ti^{3+} and O_v act as electron traps and inhibit the recombination process (equations (3.10) and (3.11)). Furthermore, the photogenerated electron could be transferred to GO as well (equation (3.12)). The electrons localized in CB, Ti^{3+}/O_v or GO can be transferred to an oxygen molecule to produce superoxide anion (equations (3.10)–(3.12)) [73,102]

$$e^-_{\mathrm{CB}} \rightarrow \ e^-(\mathrm{Ti}^{3+}) \ + \ \mathrm{O_2} \rightarrow \mathrm{O_2^{\bullet -}}, \tag{3.10}$$

$$e^-_{\mathrm{CB}} \rightarrow \ e^-(\mathrm{O}_v) \ + \ \mathrm{O_2} \rightarrow \mathrm{O_2^{\bullet -}} \tag{3.11}$$

and

$$e^-_{\mathrm{CB}} \rightarrow \ e^-(\mathrm{GO}) + \ \mathrm{O_2} \rightarrow \mathrm{O_2^{\bullet -}}. \tag{3.12}$$

In this stage, more reactive oxygen species can be generated and the degradation of pollutant begins [102,103] (figure 12)

$$\mathrm{O_2^{\bullet -}} + \ \mathrm{H_2O} \rightarrow \mathrm{OH^{\bullet}}. \tag{3.13}$$

4. Conclusion

The present study synthesized TiO_2–GO composites and studied the natural dye sensitization of TiO_2–GO thin films with natural dyes extracted from *B. guineensis*. The spectroscopic, morphological and structural characterization of the composites was presented in detail. All results corroborated that the presence of GO and the natural sensitizer have an important synergistic effect on the physical chemistry properties of the composites. A red shift in the band gap values was detected after GO incorporation and natural dye sensitization from 3.21 eV (TiO_2) to 2.45 eV (D-TiO_2–GO). Results showed that the photodegradation yield of D-TiO_2–GO was greater than that of TiO_2–CO, indicating that GO could facilitate the separation of charge carriers suppressing the recombination of charge carriers, and the photodegradation yield was improved by the presence of GO and natural dye sensitization. The best photodegradation yield was reached by D-TiO_2–GO, indicating that the presence of GO has an important synergistic effect in conjunction with the natural sensitizer. Finally, the results corroborate that natural sensitizers are an economic, harmless and promising source of dyes to be used in semiconductor sensitization.

Data accessibility. Our data are deposited at the Dryad Digital Repository: http://dx.doi.org/10.5061/dryad.mc810bq [104].

Authors' contributions. W.V. and C.D.-U. both conceived the original idea and directed the research; C.G. synthesized and characterized GO; A.R. synthesized the composites; A.R. and P.Q. characterized the composites. All authors contributed to the writing and editing of the manuscript.

Competing interests. We declare that we have no competing interests.
Funding. W.V., A.R., C.D-U. and C.G. get financial support from Universidad del Atlántico. P.Q. gets financial support from IPN-CINVESTAV.
Acknowledgements. The authors thank Centro de Investigación y de Estudios Avanzados del IPN-CINVESTAV for supporting all physical chemistry characterization measurements. W.V. thanks Universidad del Atlántico (Project Code CB20-FGI2016, Res. Rec. No. 000721 - 10/05/2017).

References

1. Borges GA, Silva LP, Penido JA, de Lemos LR, Mageste AB, Rodrigues GD. 2016 A method for dye extraction using an aqueous two-phase system: effect of co-occurrence of contaminants in textile industry wastewater. *J. Environ. Manage.* **183**, 196–203. (doi:10.1016/J.JENVMAN.2016.08.056)
2. Khataee AR, Vafaei F, Jannatkhah M. 2013 Biosorption of three textile dyes from contaminated water by filamentous green algal *Spirogyra* sp.: kinetic, isotherm and thermodynamic studies. *Int. Biodeterior. Biodegradation* **83**, 33–40. (doi:10.1016/J.IBIOD.2013.04.004)
3. Dong S, Feng J, Fan M, Pi Y, Hu L, Han X, Liu M, Sun J, Sun J. 2015 Recent developments in heterogeneous photocatalytic water treatment using visible light-responsive photocatalysts: a review. *RSC Adv.* **5**, 14 610–14 630. (doi:10.1039/C4RA13734E)
4. Liu B, Zhao X, Terashima C, Fujishima A, Nakata K. 2014 Thermodynamic and kinetic analysis of heterogeneous photocatalysis for semiconductor systems. *Phys. Chem. Chem. Phys.* **16**, 8751. (doi:10.1039/c3cp55317e)
5. Kant R. 2012 Textile dyeing industry an environmental hazard. *Nat. Sci.* **4**, 22–26. (doi:10.4236/ns.2012.41004)
6. Rosales A *et al.* 2018 SiO_2@TiO_2 coating: synthesis, physical characterization and photocatalytic evaluation. *Coatings* **8**, 120. (doi:10.3390/coatings8040120)
7. Diasanayake MAKL, Senadeera GKR, Sarangika HNM, Ekanayake PMPC, Thotawattage CA, Divarathne HKDWMNR, Kumari JMKW. 2016 TiO_2 as a low cost, multi functional material. *Mater. Today Proc.* **3S**, S40–S47. (doi:10.1016/j.matpr.2016.01.006)
8. Danish M, Ambreen S, Chauhan A, Pandey A. 2015 Optimization and comparative evaluation of optical and photocatalytic properties of TiO_2 thin films prepared via sol–gel method. *J. Saudi Chem. Soc.* **19**, 557–562. (doi:10.1016/J.JSCS.2015.05.010)
9. Hamad H, Abd El-Latif M, Kashyout AE-H, Sadik W, Feteha M. 2015 Synthesis and characterization of core–shell–shell magnetic ($CoFe_2O_4$–SiO–TiO_2 nanocomposites and TiO_2 nanoparticles for the evaluation of photocatalytic activity under UV and visible irradiation. *New J. Chem.* **39**, 3116–3128. (doi:10.1039/C4NJ01821D)
10. Ranasinghe CSK, Vequizo JJM, Yamakata A. 2018 Fabrication of robust TiO_2 thin films by atomized spray pyrolysis deposition for photoelectrochemical water oxidation. *J. Photochem. Photobiol. A Chem.* **358**, 320–326. (doi:10.1016/J.JPHOTOCHEM.2017.09.006)
11. Alotaibi AM, Sathasivam S, Williamson BAD, Kafizas A, Sotelo-Vazquez C, Taylor A, Scanlon DO, Parkin IP. 2018 Chemical vapor deposition of photocatalytically active pure brookite TiO_2 thin films. *Chem. Mater.* **30**, 1353–1361. (doi:10.1021/acs.chemmater.7b04944)
12. Yuan R, Zhou B, Hua D, Shi C, Ma L. 2014 Effect of metal-ion doping on the characteristics and photocatalytic activity of TiO_2 nanotubes for the removal of toluene from water. *Water Sci. Technol.* **69**, 1697–1704. (doi:10.2166/wst.2014.071)
13. Yalçın, Kılıç M, Çinar Z. 2018 The role of non-metal doping in TiO_2 photocatalysis. *J. Adv. Oxid. Technol.* **13**, 281–296. (doi:10.1515/jaots-2010-0306)
14. Qin D-D, Wang Q-H, Chen J, He C-H, Li Y, Wang C-H, Quan J-J, Tao C-L, Lu X-Q. 2017 Phosphorus-doped TiO_2 nanotube arrays for visible-light-driven photoelectrochemical water oxidation. *Sustain. Energy Fuels* **1**, 248–253. (doi:10.1039/C6SE00045B)
15. Jung H-Y, Yeo I-S, Kim T-U, Ki H-C, Gu H-B. 2018 Surface plasmon resonance effect of silver nanoparticles on a TiO_2 electrode for dye-sensitized solar cells. *Appl. Surf. Sci.* **432**, 266–271. (doi:10.1016/J.APSUSC.2017.04.237)
16. Talebi S, Chaibakhsh N, Moradi-Shoeili Z. 2017 Application of nanoscale ZnS/TiO_2 composite for optimized photocatalytic decolorization of a textile dye. *J. Appl. Res. Technol.* **15**, 378–385. (doi:10.1016/J.JART.2017.03.007)
17. Li D, Wang S, Wang J, Zhang X, Liu S. 2013 Synthesis of CdTe/TiO_2 nanoparticles and their photocatalytic activity. *Mater. Res. Bull.* **48**, 4283–4286. (doi:10.1016/J.MATERRESBULL.2013.06.052)
18. Xu J, Wang W, Sun S, Wang L. 2012 Enhancing visible-light-induced photocatalytic activity by coupling with wide-band-gap semiconductor: a case study on Bi_2WO_6/TiO_2. *Appl. Catal. B Environ.* **111–112**, 126–132. (doi:10.1016/J.APCATB.2011.09.025)
19. Shahid M, Shahid-ul-Islam MF. 2013 Recent advancements in natural dye applications: a review. *J. Clean. Prod.* **53**, 310–331. (doi:10.1016/J.JCLEPRO.2013.03.031)
20. Ghann W, Kang H, Sheikh T, Yadav S, Chavez-Gil T, Nesbitt F, Uddin J. 2017 Fabrication, optimization and characterization of natural dye sensitized solar cell. *Sci. Rep.* **7**, 41470. (doi:10.1038/srep41470)
21. Reddy KR, Karthik KV, Prasad SBB, Soni SK, Jeong HM, Raghu AV. 2016 Enhanced photocatalytic activity of nanostructured titanium dioxide/polyaniline hybrid photocatalysts. *Polyhedron* **120**, 169–174. (doi:10.1016/J.POLY.2016.08.029)
22. Yuvapragasam A, Muthukumarasamy N, Agilan S, Velauthapillai D, Senthil TS, Sundaram S. 2015 Natural dye sensitized TiO_2 nanorods assembly of broccoli shape based solar cells. *J. Photochem. Photobiol. B Biol.* **148**, 223–231. (doi:10.1016/J.JPHOTOBIOL.2015.04.017)
23. Sathyajothi S, Jayavel R, Dhanemozhi AC. 2017 The fabrication of natural dye sensitized solar cell (Dssc) based on TiO_2 using henna and beetroot dye extracts. *Mater. Today Proc.* **4**, 668–676. (doi:10.1016/J.MATPR.2017.01.071)
24. Buddee S, Wongnawa S, Sriprang P, Sriwong C. 2014 Curcumin-sensitized TiO_2 for enhanced photodegradation of dyes under visible light. *J. Nanoparticle Res.* **16**, 2336. (doi:10.1007/s11051-014-2336-z)
25. Zyoud A, Zaatar N, Saadeddin I, Helal MH, Campet G, Hakim M, DaeHoon PHSH. 2011 Alternative natural dyes in water purification: anthocyanin as TiO_2-sensitizer in methyl orange photo-degradation. *Solid State Sci.* **13**, 1268–1275. (doi:10.1016/j.solidstatesciences.2011.03.020)
26. Díaz-Uribe C, Vallejo W, Campos K, Solano W, Andrade J, Muñoz-Acevedo A, Schott E, Zarate X. 2018 Improvement of the photocatalytic activity of TiO_2 using Colombian Caribbean species (*Syzygium cumini*) as natural sensitizers: experimental and theoretical studies. *Dye. Pigment.* **150**, 370–376. (doi:10.1016/J.DYEPIG.2017.12.027)
27. Osorio C, Acevedo B, Hillebrand S, Carriazo J, Winterhalter P, Morales AL. 2010 Microencapsulation by spray-drying of anthocyanin pigments from corozo (*Bactris guineensis*) fruit. *J. Agric. Food Chem.* **58**, 6977–6985. (doi:10.1021/jf100536g)
28. Gao Y, Hu M, Mi B. 2014 Membrane surface modification with TiO_2–graphene oxide for enhanced photocatalytic performance. *J. Memb. Sci.* **455**, 349–356. (doi:10.1016/J.MEMSCI.2014.01.011)
29. Alam U, Fleisch M, Kretschmer I, Bahnemann D, Muneer M. 2017 One-step hydrothermal synthesis of Bi-TiO_2 nanotube/graphene composites: an efficient photocatalyst for spectacular degradation of organic pollutants under visible light irradiation. *Appl. Catal. B Environ.* **218**, 758–769. (doi:10.1016/J.APCATB.2017.06.016)
30. Gunnagol RM, Rabinal MHK. 2018 TiO_2-graphene nanocomposites for effective photocatalytic degradation of Rhodamine-B dye. *ChemistrySelect* **3**, 2578–2585. (doi:10.1002/slct.201703081)
31. Yang Y, Xu L, Wang H, Wang W, Zhang L. 2016 TiO_2/graphene porous composite and its

photocatalytic degradation of methylene blue. *Mater. Des.* **108**, 632–639. (doi:10.1016/J.MATDES.2016.06.104)

32. Stengl V, Bakardjieva S, Grygar TM, Bludská J, Kormunda M. 2013 TiO_2-graphene oxide nanocomposite as advanced photocatalytic materials. *Chem. Cent. J.* **7**, 41. (doi:10.1186/1752-153X-7-41)
33. Fan J, Grande CD, Rodrigues DF. 2017 Biodegradation of graphene oxide-polymer nanocomposite films in wastewater. *Environ. Sci. Nano* **4**, 1808–1816. (doi:10.1039/C7EN00396J)
34. Perez JVD, Nadres ET, Nguyen HN, Dalida MLP, Rodrigues DF. 2017 Response surface methodology as a powerful tool to optimize the synthesis of polymer-based graphene oxide nanocomposites for simultaneous removal of cationic and anionic heavy metal contaminants. *RSC Adv.* **7**, 18 480–18 490. (doi:10.1039/C7RA00750G)
35. Cao SY, Chen CS, Ning XT, Zeng B, Xie XD, Chen XH, Wei SS, Mei YP, Zhao GJ. 2013 Preparation and photocatalytic property of graphene/TiO_2 composite powder. *Integr. Ferroelectr.* **145**, 40–45. (doi:10.1080/10584587.2013.788362)
36. Quintana P, Tiesler V, Conde M, Trejo-tzab R, Bolio C, Alvarado-gil JJ, Aguilar D. 2015 Spectrochemical characterization of red pigments used in classic period Maya funerary practices. *Archaeometry* **57**, 1045–1059. (doi:10.1111/arcm.12144)
37. Mills A. 2012 An overview of the methylene blue ISO test for assessing the activities of photocatalytic films. *Appl. Catal. B Environ.* **128**, 144–149. (doi:10.1016/J.APCATB.2012.01.019)
38. Lowell S, Shields JE. 1991 *Powder surface area and porosity*, 3rd edn. New York, NY: Springer Science and Business Media.
39. Lavanya T, Dutta M, Satheesh K. 2016 Graphene wrapped porous tubular rutile TiO_2 nanofibers with superior interfacial contact for highly efficient photocatalytic performance for water treatment. *Sep. Purif. Technol.* **168**, 284–293. (doi:10.1016/j.seppur.2016.05.059)
40. Pan N, Guan D, Yang Y, Huang Z, Wang R, Jin Y, Xia C. 2014 A rapid low-temperature synthetic method leading to large-scale carboxyl graphene. *Chem. Eng. J.* **236**, 471–479. (doi:10.1016/J.CEJ.2013.10.060)
41. Ganguly A, Sharma S, Papakonstantinou P, Hamilton J. 2011 Probing the thermal deoxygenation of graphene oxide using high-resolution in situ X-ray-based spectroscopies. *J. Phys. Chem. C* **115**, 17 009–17 019. (doi:10.1021/jp203741y)
42. Nagaraju P, Alsalme A, Alswieleh A, Jayavel R. 2018 Facile in-situ microwave irradiation synthesis of TiO_2/graphene nanocomposite for high-performance supercapacitor applications. *J. Electroanal. Chem.* **808**, 90–100. (doi:10.1016/J.JELECHEM.2017.11.068)
43. Chang BYS, Huang NM, Nor An'amt M, Marlinda AR, Norazriena Y, Muhamad MR, Harrison I, Lim HN, Chia CH. 2012 Facile hydrothermal preparation of titanium dioxide decorated reduced graphene oxide nanocomposite. *Int. J. Nanomed.* **7**, 3379. (doi:10.2147/IJN.S28189)
44. Xie Y, Hwan S, Seung H, Yoo H, Sung A, Cho O. 2009 Synthesis and photocatalytic activity of anatase TiO_2 nanoparticles-coated carbon nanotubes. *Nano. Res. Lett.* **5**, 603–607. (doi:10.1007/s11671-009-9513-5)
45. Mikami M, Nakamura S, Kitao O, Arakawa H. 2002 Lattice dynamics and dielectric properties of TiO_2 anatase: a first-principles study. *Phys. Rev. B* **66**, 155213. (doi:10.1103/PhysRevB.66.155213)
46. Belka R. 2017 Using the principal component analysis method in studies of the TiO_2 Raman spectra. In *Proc. SPIE 10445, Photonics Applications in Astronomy, Communications, Industry, and High Energy Physics Experiments* (eds RS Romaniuk, M Linczuk), p. 104454Q. (doi:10.1117/12.2279987)
47. Chen JS, Luan D, Li CM, Boey FYC, Qiao S, Lou XW. 2010 TiO_2 and SnO_2@TiO_2 hollow spheres assembled from anatase TiO_2 nanosheets with enhanced lithium storage properties. *Chem. Commun.* **46**, 8252. (doi:10.1039/c0cc02973d)
48. Tseng I-H, Sung Y-M, Chang P-Y, Lin S-W. 2017 Photocatalytic performance of titania nanosheets templated by graphene oxide. *J. Photochem. Photobiol. A Chem.* **339**, 1–11. (doi:10.1016/J.JPHOTOCHEM.2017.01.036)
49. Ferrari AC, Basko DM. 2013 Raman spectroscopy as a versatile tool for studying the properties of graphene. *Nat. Nanotechnol.* **8**, 235–246. (doi:10.1038/nnano.2013.46)
50. Jiang K-C, Xin S, Lee J-S, Kim J, Xiao X-L, Guo Y-G. 2012 Improved kinetics of $LiNi_{1/3}Mn_{1/3}Co_{1/3}O_2$ cathode material through reduced graphene oxide networks. *Phys. Chem. Chem. Phys.* **14**, 2934. (doi:10.1039/c2cp23363k)
51. Couzi M, Bruneel J-L, Talaga D, Bokobza L. 2016 A multi wavelength Raman scattering study of defective graphitic carbon materials: the first order Raman spectra revisited. *Carbon NY* **107**, 388–394. (doi:10.1016/J.CARBON.2016.06.017)
52. Bokobza L, Bruneel J-L, Couzi M. 2015 Raman spectra of carbon-based materials (from graphite to carbon black) and of some silicone composites. *Carbon* **1**, 77–94. (doi:10.3390/c1010077)
53. Naumenko D, Snitka V, Snopok B, Arpiainen S, Lipsanen H. 2012 Graphene-enhanced Raman imaging of TiO_2 nanoparticles. *Nanotechnology* **23**, 465703. (doi:10.1088/0957-4484/23/46/465703)
54. Martins FEH, Moutinho MVO, Stavale F, Lucchese MM, Capaz RB, Achete CA, Jorio A. 2010 Evolution of the Raman spectra from single-, few-, and many-layer graphene with increasing disorder. *Phys. Rev. B* **82**, 125429. (doi:10.1103/PhysRevB.82.125429)
55. Cançado LG *et al.* 2011 Quantifying defects in graphene via Raman spectroscopy at different excitation energies. *Nano Lett.* **11**, 3190–3196. (doi:10.1021/nl201432g)
56. Mali SS, Shinde PS, Betty CA, Bhosale PN, Lee WJ, Patil PS. 2011 Nanocoral architecture of TiO_2 by hydrothermal process: synthesis and characterization. *Appl. Surf. Sci.* **257**, 9737–9746. (doi:10.1016/J.APSUSC.2011.05.119)
57. Rasoulnezhad H, Hosseinzadeh G, Yekrang J. 2018 Preparation and characterization of nanostructured S and Fe co-doped TiO_2 thin film by ultrasonic-assisted spray pyrolysis method. *J. Nanostruct.* **8**, 251–258. (doi:10.22052/JNS.2018.03.4)
58. Qiu J, Lai C, Wang Y, Li S, Zhang S. 2014 Resilient mesoporous TiO_2/graphene nanocomposite for high rate performance lithium-ion batteries. *Chem. Eng. J.* **256**, 247–254. (doi:10.1016/J.CEJ.2014.06.116)
59. Chun H-H, Jo W-K. 2016 Adsorption and photocatalysis of 2-ethyl-1-hexanol over graphene oxide–TiO_2 hybrids post-treated under various thermal conditions. *Appl. Catal. B Environ.* **180**, 740–750. (doi:10.1016/j.apcatb.2015.07.021)
60. Liu S, Sun H, Liu S, Wang S. 2013 Graphene facilitated visible light photodegradation of methylene blue over titanium dioxide photocatalysts. *Chem. Eng. J.* **214**, 298–303. (doi:10.1016/J.CEJ.2012.10.058)
61. León A *et al.* 2017 FTIR and Raman characterization of TiO_2 nanoparticles coated with polyethylene glycol as carrier for 2-methoxyestradiol. *Appl. Sci.* **7**, 49. (doi:10.3390/app7010049)
62. Ali G, Leila V, Nader NMR. 2015 A new application of nano-graphene oxide (NGO) as a heterogeneous catalyst in oxidation of alcohols types. *Chem. J.* **1**, 151–158.
63. Nguyen-Phan T-D, Pham VH, Shin EW, Pham H-D, Kim S, Chung JS, Kim EJ, Hur SH. 2011 The role of graphene oxide content on the adsorption-enhanced photocatalysis of titanium dioxide/graphene oxide composites. *Chem. Eng. J.* **170**, 226–232. (doi:10.1016/J.CEJ.2011.03.060)
64. Vanessa B, Henry B, Marco CHT. 2014 Isolation and chemical characterization of two new anthocyanin pigments from Güiscoyol (*Bactris guineensis*) fruit. *Eur. J. Sci. Res.* **127**, 369–381.
65. Chang H, Kao M-J, Chen T-L, Chen C-H, Cho K-C, Lai X-R. 2013 Characterization of natural dye extracted from wormwood and purple cabbage for dye-sensitized solar cells. *Int. J. Photoenergy* **2013**, 1–8. (doi:10.1155/2013/159502)
66. Park Y, Kim W, Monllor-Satoca D, Tachikawa T, Majima T, Choi W. 2013 Role of interparticle charge transfers in agglomerated photocatalyst nanoparticles: demonstration in aqueous suspension of dye-sensitized TiO_2. *J. Phys. Chem. Lett.* **4**, 189–194. (doi:10.1021/jz301881d)
67. Lakshminarasimhan N, Bokare AD, Choi W. 2012 Effect of agglomerated state in mesoporous TiO_2 on the morphology of photodeposited Pt and photocatalytic activity. *J. Phys. Chem. C* **116**, 17 531–17 539. (doi:10.1021/jp303118q)
68. Ryu J, Kim S, Kim H, Jo E-H, Kim YK, Kim M, Jang HD. 2015 Self-assembled TiO_2 agglomerates hybridized with reduced-graphene oxide: a high-performance hybrid photocatalyst for solar energy conversion. *Chem. Eng. J.* **262**, 409–416. (doi:10.1016/j.cej.2014.10.001)
69. Amir A, Bunyod A, Jeonghwan L, Heung-Woo J, Soon-Wook JSK. 2013 X-ray photoelectron spectroscopy characterization of Fe doped TiO_2 photocatalyst. *Int. J. Mater. Mech. Manuf.* **1**, 294–296. (doi:10.7763/IJMMM.2013.V1.63)
70. Chowdhury S, Parshetti GK, Balasubramanian R. 2015 Post-combustion CO_2 capture using mesoporous TiO_2/graphene oxide

nanocomposites. *Chem. Eng. J.* **263**, 374–384. (doi:10.1016/J.CEJ.2014.11.037)

71. Yan Z, Gong W, Chen Y, Duan D, Li J, Wang W, Wang J. 2014 Visible-light degradation of dyes and phenols over mesoporous titania prepared by using anthocyanin from red radish as template. *Int. J. Photoenergy* **2014**, 1–10. (doi:10.1155/2014/968298)
72. Xing M, Shen F, Qiu B, Zhang J. 2015 Highly-dispersed boron-doped graphene nanosheets loaded with TiO_2 nanoparticles for enhancing CO_2 photoreduction. *Sci. Rep.* **4**, 6341. (doi:10.1038/srep06341)
73. Qingzhe Z, Nan B, Xinqiang W, Xinde H, Xinhan MMC. 2016 Advanced fabrication of chemically bonded graphene/TiO_2 continuous fibers with enhanced broadband photocatalytic properties and involved mechanisms exploration. *Sci. Rep.* **6**, 1–15. (doi:10.1038/srep38066)
74. Rasoulnezhad H, Hosseinzadeh G, Hosseinzadeh R, Ghasemian N. 2018 Preparation of transparent nanostructured N-doped TiO_2 thin films by combination of sonochemical and CVD methods with visible light photocatalytic activity. *J. Adv. Ceram.* **7**, 185–196. (doi:10.1007/s40145-018-0270-8)
75. Zhang X-Y, Li H-P, Cui X-L, Lin Y. 2010 Graphene/TiO_2 nanocomposites: synthesis, characterization and application in hydrogen evolution from water photocatalytic splitting. *J. Mater. Chem.* **20**, 2801. (doi:10.1039/b917240h)
76. Zschoerper NP, Katzenmaier V, Vohrer U, Haupt M, Oehr C, Hirth T. 2009 Analytical investigation of the composition of plasma-induced functional groups on carbon nanotube sheets. *Carbon NY* **47**, 2174–2185. (doi:10.1016/J.CARBON.2009.03.059)
77. Jiang G, Lin Z, Chen C, Zhu L, Chang Q, Wang N, Wei W, Tang H. 2011 TiO_2 nanoparticles assembled on graphene oxide nanosheets with high photocatalytic activity for removal of pollutants. *Carbon NY* **49**, 2693–2701. (doi:10.1016/J.CARBON.2011.02.059)
78. Zhang J, Pan C, Fang P, Wei J, Xiong R. 2010 Mo + C codoped TiO_2 using thermal oxidation for enhancing photocatalytic activity. *ACS Appl. Mater. Interfaces* **2**, 1173–1176. (doi:10.1021/am100011c)
79. Gao Y, Pu X, Zhang D, Ding G, Shao X, Ma J. 2012 Combustion synthesis of graphene oxide–TiO_2 hybrid materials for photodegradation of methyl orange. *Carbon NY* **50**, 4093–4101. (doi:10.1016/J.CARBON.2012.04.057)
80. Hu Z, Huang Y, Sun S, Guan W, Yao Y, Tang P, Li C. 2012 Visible light driven photodynamic anticancer activity of graphene oxide/TiO_2 hybrid. *Carbon NY* **50**, 994–1004. (doi:10.1016/J.CARBON.2011.10.002)
81. Madhusudan RK, Manorama SV, Ramachandra RA. 2003 Bandgap studies on anatase titanium dioxide nanoparticles. *Mater. Chem. Phys.* **78**, 239–245. (doi:10.1016/S0254-0584(02) 00343-7)
82. Ahliha AH, Nurosyid F, Supriyanto A, Kusumaningsih T. 2018 Optical properties of anthocyanin dyes on TiO_2 as photosensitizers for application of dye-sensitized solar cell (DSSC). *IOP Conf. Ser. Mater. Sci. Eng.* **33**, 012018. (doi:10.1088/1757-899X/333/1/012018)
83. Okoli LU, Ozuomba JO, Ekpunobi AJ. 2012 Anthocyanin-dyed TiO_2 electrode and its performance on dye-sensitized solar cell. *Res. J. Recent Sci.* **1**, 22–27.
84. Simmons EL. 1972 Relation of the diffuse reflectance remission function to the fundamental optical parameters. *Opt. Acta Int. J. Opt.* **19**, 845–851. (doi:10.1080/713818505)
85. Tauc J, Grigorovici R, Vancu A. 1966 Optical properties and electronic structure of amorphous germanium. *Phys. Status Solidi* **15**, 627–637. (doi:10.1002/pssb.19660150224)
86. Viezbicke BD, Patel S, Davis BE, Birnie DP. 2015 Evaluation of the Tauc method for optical absorption edge determination: ZnO thin films as a model system. *Phys. Status Solidi* **252**, 1700–1710. (doi:10.1002/pssb.201552007)
87. Pal M, Pal U, Jiménez JMGY, Pérez-Rodríguez F. 2012 Effects of crystallization and dopant concentration on the emission behavior of TiO_2:Eu nanophosphors. *Nanoscale Res. Lett.* **7**, 1. (doi:10.1186/1556-276X-7-1)
88. Valencia HSH, Marín SJM, Restrepo VGM. 2010 Study of the bandgap of synthesized titanium dioxide nanoparticules using the sol-gel method and a hydrothermal treatment. *Univ. Antioquia* **4**, 9–14. (doi:10.2174/1874088X01004010009)
89. Zhang H, Lv X, Li Y, Wang Y, Li J. 2010 P25-graphene composite as a high performance photocatalyst. *ACS Nano* **4**, 380–386. (doi:10.1021/nn901221k)
90. Zhang Y, Tang Z-R, Fu X, Xu Y-J. 2010 TiO_2—graphene nanocomposites for gas-phase photocatalytic degradation of volatile aromatic pollutant: is TiO_2—graphene truly different from other TiO_2—carbon composite materials? *ACS Nano* **4**, 7303–7314. (doi:10.1021/nn1024219)
91. Shao X, Lu W, Zhang R, Pan F. 2013 Enhanced photocatalytic activity of TiO_2-C hybrid aerogels for methylene blue degradation. *Sci. Rep.* **3**, 3018. (doi:10.1038/srep03018)
92. San EACM, Enriquez EP. 2013 Graphene–anthocyanin mixture as photosensitizer for dye-sensitized solar cell. *Sol. Energy* **98**, 392–399. (doi:10.1016/J.SOLENER.2013.09.036)
93. Kazmi SA, Hameed S, Ahmed AS, Arshad M, Azam A. 2017 Electrical and optical properties of graphene-TiO_2 nanocomposite and its applications in dye sensitized solar cells (DSSC). *J. Alloys Compd.* **691**, 659–665. (doi:10.1016/J.JALLCOM.2016.08.319)
94. Sedghi R, Heidari F. 2016 A novel & effective visible light-driven TiO_2/magnetic porous graphene oxide nanocomposite for the degradation of dye pollutants. *RSC Adv.* **6**, 49 459–49 468. (doi:10.1039/C6RA02827F)
95. Konstantinou IK, Albanis TA. 2004 TiO_2-assisted photocatalytic degradation of azo dyes in aqueous solution: kinetic and mechanistic investigations a review. *Appl. Catal. B Environ.* **49**, 1–14. (doi:10.1016/j.apcatb.2003.11.010)
96. Khataee AR, Fathinia M, Aber S. 2010 Kinetic modeling of liquid phase photocatalysis on supported TiO_2 nanoparticles in a rectangular flat-plate photoreactor. *Ind. Eng. Chem. Res.* **49**, 12 358–12 364. (doi:10.1021/ie101997u)
97. Rasoulnezhad H, Hosseinzadeh G, Ghasemian N, Hosseinzadeh R, Keihan AH. 2018 Transparent nanostructured Fe-doped TiO_2 thin films prepared by ultrasonic assisted spray pyrolysis technique. *Mater. Res. Express* **5**, 056401. (doi:10.1088/2053-1591/aabe5e)
98. Yang C, Dong W, Cui G, Zhao Y, Shi X, Xia X, Tang B, Wang W. 2017 Highly-efficient photocatalytic degradation of methylene blue by PoPD-modified TiO_2 nanocomposites due to photosensitization-synergetic effect of TiO_2 with PoPD. *Sci. Rep.* **7**, 3973. (doi:10.1038/s41598-017-04398-x)
99. Jaihindh DP, Chen C-C, Fu Y-P. 2018 Reduced graphene oxide-supported Ag-loaded Fe-doped TiO_2 for the degradation mechanism of methylene blue and its electrochemical properties. *RSC Adv.* **8**, 6488–6501. (doi:10.1039/c7ra13418e)
100. Sohail M, Xue H, Jiao Q, Li H, Khan K, Wang S, Zhao Y. 2017 Synthesis of well-dispersed TiO_2@reduced graphene oxide (rGO) nanocomposites and their photocatalytic properties. *Mater. Res. Bull.* **90**, 125–130. (doi:10.1016/J.MATERRESBULL.2017.02.025)
101. Vallejo LWA, Quinones SCA, Hernandez SJA. 2011 The chemistry and physics of dye-sensitized solar cells. In *Solar cells—dye-sensitized devices*. London, UK: InTech.
102. Chowdhury P, Moreira J, Gomaa H, Ray AK. 2012 Visible-solar-light-driven photocatalytic degradation of phenol with dye-sensitized TiO_2: parametric and kinetic study. *Ind. Eng. Chem. Res.* **51**, 4523–4532. (doi:10.1021/ie2025213)
103. Chatterjee D, Dasgupta S, N Rao N. 2006 Visible light assisted photodegradation of halocarbons on the dye modified TiO_2 surface using visible light. *Sol. Energy Mater. Sol. Cells* **90**, 1013–1020. (doi:10.1016/J.SOLMAT.2005.05.016)
104. Vallejo W, Rueda A, Díaz-Uribe C, Grande C, Quintana P. 2019 Data from: Photocatalytic activity of graphene oxide–TiO_2 thin films sensitized by natural dyes extracted from *Bactris guineensis*. Dryad Digital Repository. (doi:10.5061/dryad.mc810bq)